Talanta 285 (2025) 127400

Contents lists available at ScienceDirect

Talanta

journal homepage: www.elsevier.com/locate/talanta

An organic-inorganic polyacrylamide-based surface imprinted quantum dots for the impedimetric and voltammetric detection of diazepam in saliva with smartphone readout

Oluwasesan Adegoke [a,*], Kayode Oyinlola [a], Kayode Omotayo Adeniyi [a], Ojodomo J. Achadu [b], Zhugen Yang [c], Niamh Nic Daeid [a]

[a] Leverhulme Research Centre for Forensic Science, School of Science and Engineering, University of Dundee, Dundee, DD1 4HN, UK
[b] School of Health and Life Sciences, and National Horizon Centre, Teesside University, TS1 3BA, Middlesbrough, UK
[c] Faculty of Engineering and Applied Sciences, Cranfield University, Cranfield, MK43 0AL, UK

A B S T R A C T

Diazepam (DZP) is a muscle-relaxing, anxiety-relieving sedative drug; nonetheless, it is also an addictive drug that may be abused. This work reports on the development of a novel electrochemical nanosensor for diazepam using SiO_2-encapsulated-3-mercaptopropionic acid-capped AuZnCeSeS quantum dots (QDs) overcoated with a molecularly imprinted polymer (MIP) on screen-printed carbon electrodes (SPCEs). Electrochemical, spectroscopic and electron microscopic characterization of the nanomaterial and modified electrode surface was carried out and is reported herein. Specifically, electrochemical characterization of the QDs/SPCE using cyclic voltammetry (CV) revealed that the QDs exhibit a higher electrode surface area whilst electrochemical impedance spectroscopy (EIS) characterization demonstrated a lower charge transfer resistance (R_{ct}). To fabricate the electrochemical nanosensor, firstly, alloyed AuZnCeSeS QDs were synthesized in the organic phase and thereafter capped with 3-mercaptopropionic acid (MPA) via a ligand exchange reaction. The MPA-AuZnCeSeS QDs were encapsulated in a SiO_2 layer to form a SiO_2-MPA AuZnCeSeS QDs system. The QDs were drop-casted onto SPCEs to form a SiO_2-MPA AuZnCeSeS QDs/SPCE transducer interface. Organic based acrylamide, used as a functional monomer, was electropolymerized via CV on the QDs/SPCE in the presence of the diazepam template with ethylene glycol dimethacrylate as a crosslinker and 2,2′-azobis(2-methylpropionitrile) as an initiator. Under optimum experimental conditions, DZP was detected using EIS and square wave voltammetry (SWV). Using a portable potentiostat and a hand-held smartphone-based potentiostat, DZP was quantitatively detected in saliva using the MIP@QDs/SPCE with a limit of detection (LOD) of 2.3 μM and 2.7 μM, respectively. The LOD for DZP from SWV analysis was 1.0 μM.

1. Introduction

Diazepam (DZP) is known as one of the most commonly prescribed 1,4-benzodiazepines that is used therapeutically to treat muscular spasms, alcohol withdrawal, epilepsy, insomnia and anxiety. It is also marketed by its generic name, Valium® [1,2]. Confusion, ataxia, fatigue and drowsiness are examples of side effects experienced from the use of DZP. DZP use, alongside other depressant substances have been reported to lead to increased absorption rates and sedative effects [3–5]. These effects have led to DZP being used alongside other drugs such as opioids or as an adulterant for some herbal medicines, as well as being implicated in drug-facilitated sexual assault (DFSA) [6–8]. The increased availability and the falling price of DZP on the illicit drug market, have also contributed to the abuse of the drug [9,10] These contributing factors have led to the development of a range of analytical sensor systems for the direct detection of DZP.

Reported methods for DZP detection include chromatographic techniques such as high-performance liquid chromatography (HPLC) [11] and gas chromatography/mass spectrometry (GCMS) [12] as well as electrochemical [13,14], capillary electrophoresis [15] and spectrofluorimetric methods [16,17]. Chromatography techniques can be time consuming, expensive, require highly trained personnel to operate and are also not always suitable for frontline use. Electrochemical methods, on the other hand, are very promising due to the various portable hand-held potentiostats available on the market which facilitate the fabrication of sensors on screen-printed electrodes suitable for the field detection of target compounds of interest. This facilitates an opportunity for the development of rapid, portable, and sensitive sensor systems for target drug compounds.

To date, there are several nanomaterials used in mainstream sensors research and amongst the diverse types, semiconductor quantum dot (QD) nanocrystals have attracted considerable interest. QDs are zero-dimensional nanostructured materials that are mainly composed of elements in groups II-VI, III-V and IV-VI of the periodic table [18]. Due to

* Corresponding author. Leverhulme Research Centre for Forensic Science, School of Science & Engineering, University of Dundee, Dundee, DD1 4HN, UK.
E-mail address: o.adegoke@dundee.ac.uk (O. Adegoke).

https://doi.org/10.1016/j.talanta.2024.127400
Received 6 August 2024; Received in revised form 25 November 2024; Accepted 15 December 2024
Available online 17 December 2024
0039-9140/© 2024 The Authors. Published by Elsevier B.V. This is an open access article under the CC BY license (http://creativecommons.org/licenses/by/4.0/).

their anisotropic geometry and size confinement properties, QDs not only possess the properties of bulk semiconductor materials, but also exhibit catalytic, magnetic, phytochemical, optoelectric and piezoelectric properties [19]. These unique properties, coupled with high surface area-to-volume ratio, excellent photostability, high resistance to photodegradation and size-dependent absorption and fluorescence emission properties, have rendered QDs an attractive material for a wide range of applications including sensing [20], catalysis [21], photovoltaic [22], solar cells [23], and energy storage and conversion [24].

In the area of sensing, QDs have attracted interest as nanotags [25] and/or as material components of nanocomposites [26] to boost the performance of electrochemical sensor systems. To develop an accurate electrochemical nanosensor, consideration must be given to (i) the material tag to be used to generate the required sensitivity, (ii) the working electrode surface modification and (iii) the type of receptor needed to achieve the required selectivity. QDs serve the purpose of being used as nanotags to boost the electrochemical sensor sensitivity and also as a substrate to host the receptor where the required selectivity can be achieved.

Amongst the diverse types of receptors used in mainstream sensor and biosensor research, molecularly imprinted polymers (MIPs), known as "synthetic antibodies" have attracted significant interest [27]. MIPs are porous cross-lined polymers with cavities that are specific in shape and size to the imprinted template (target of interest). The functional groups embedded within the MIP structure are known to bind to the target analyte via electrostatic interaction, hydrophobicity or hydrogen bonding, to aid effective affinity interaction. The thermal stability, reusability, affinity, flexibility, low-cost, simple preparation and rigidity of MIPs makes them a widely used receptor in mainstream sensor research [27]. Furthermore, the rigid properties of MIPs are what ensures that the original shape and size of the imprinted sites are retained after the template has been removed. Whilst on the other hand, the flexible property of MIP is what endows the material with the required brittleness and excellent mass transfer efficiency [27]. Thus, the combination of QDs (as nanotag and/or substrate) and MIP (as receptor) makes an excellent match [28–31] for the development of highly efficient and accurate electrochemical sensor system for the target DZP.

This study therefore reports on the novel fabrication of electropolymerized SiO_2-encapsulated quintenary Au–Zn–Ce–Se–S QDs@MIP nanosensor system for the direct detection of DZP. AuZnCeSeS QDs was chosen due to the inherent electrocatalytic properties which arises from the synergistic contributions of Au, Ce, Zn, Se, and S. Au within the QDs structure have excellent conductivity and the ability to stabilize intermediate redox species which will enhance the efficiency of the redox process [32]. Ce with its $[Xe]4f^15d^16s^2$ electronic configuration, will facilitate its role as an electronic modulator, enabling charge transfer pathways at near the Fermi level optimising electron distribution and boosting electrocatalytic performance [33]. The Ce^{3+}/Ce^{4+} redox couple, enables reversible switching between oxidation states because of flexibility as a consequence of the close energy levels of Ce's 4f and 5d orbitals and the low potential energy barrier for electron density redistribution. The electronic differences between Ce^{3+} ($4f^15d^o$) and Ce^{4+} ($4f^o5d^o$) will influence the charge distribution around the Au and, as a consequence, modulate the catalytic behaviour [33]. Selenium and sulphur, as chalcogen elements, further enhance the QDs' performance by modifying their electronic and chemical properties. This reduces the overpotentials required for reactions, improving the interaction with target molecules [32]. Zinc will stabilize the quantum dot structure, preventing aggregation and maintaining surface integrity [32]. The combined effect of the conductive gold component and the semiconductor nature of the QDs, facilitates efficient electron and ion transfer, lowering activation energy and increasing redox efficiency. Collectively, these properties make AuZnCeSeS QDs a versatile material for electrochemical sensing applications. SiO_2–AuZnCeSeS QDs were drop-casted on a screen-printed carbon electrode (SPCE) and used as signal tag to enhance the sensitivity of the electrochemical sensor system. Electroploymerization using cyclic voltammetry (CV) in the presence of a functional monomer, initiator, catalyst and the DZP template was carried out on the QDs/SPCE surface. We have demonstrated the efficacy of the MIP@QDs/SPCE nanosensor system for the direct quantitative detection of DZP in saliva and, using a hand-held smartphone-based electrochemical system, we have also demonstrated the detection of DZP with a device that could facilitate detection in the field. To the best of our knowledge, this is the first reported MIP@QDs/SPCE electrochemical nanosensor for the detection of DZP.

2. Experimental

2.1. Chemicals and materials

Acrylamide, ethylene glycol dimethacrylate (EGDMA), oleylamine, hexadecylamine, selenium (Se), sodium oleate, acrylamide, 2,2′-azobis (2-methylpropionitrile) (AIBN), sodium acetate (NaAc), tris(hydroxymethyl)aminomethane acetate salt (Trizma® Ac), trioctylyphosphine oxide (TOPO), trioctylyphosphine (TOP), oleic acid, sulphur, potassium thiocyanate (KSCN), borax, tetraethyl orthosilicate (TEOS), 2,2′-azobis (2-methylpropionitrile) (AIBN), zinc chloride, octadecene and (3-aminopropyl)triethoxysilane (APTES) were purchased from Merck. Potassium acetate (Kac), trisodium citrate, potassium ferrocyanide $K_4[Fe(CN)_6]$, potassium ferricyanide $K_3[Fe(CN)_6]$, gold (III) chloride trihydrate and myristic acid were purchased from Fisher Scientific. NaAc-Kac-Trizma Ac-KSCN-Borax (denoted as NaTKBor) buffer used in the preparation of the electrolyte solution was prepared by mixing 1 g each of NaAc, KAc, Trizma Ac, KSCN and borax in 250 mL of Milli-Q H_2O. SPCEs containing carbon as the working and counter electrode and silver (Ag) as the reference electrode as the reference electrode were purchased from Metrohm. All other chemicals were used as received.

2.2. Equipment

UV/vis absorption and fluorescence emission spectra were acquired using a Spark multimode microplate reader spectrophotometer from Tecan. Transmission electron microscopy (TEM) analysis was carried using a JEOL JEM-1200EX operated at 80 kV. Powder X-ray diffraction (PXRD) analysis was carried out using a Siemens D5000 diffractometer with Cu Kα radiation ($\lambda = 1.54056$ nm) and data were obtained in the range of 3–90° using a 0.1° 2θ step size and a 3 s count time per step with a 0.066° slit width. Scanning electron microscopy analysis (SEM) was carried out using a JEOL JSM 7400 F field emission SEM. Electrochemical measurements were carried out using a portable hand-held PalmSens4 potentiostat/galvanostat/impedance analyzer with PSTrace 5 software from PalmSens BV. For the smartphone-based application, electrochemical measurements were carried out using a Sensit Smart hand-held potentiostat with PSTouch software from PalmSens BV. The Sensit Smart potentiostat was connected to a Samsung Galaxy A53 smartphone. Analysis of data obtained from the Sensit Smart hand-held potentiostat was carried out on a laptop using PSTrace 5 software. CV analysis was carried out within the potential range of −0.3 to 0.5 V at a scan rate of 0.1 V/s. Square wave voltammetry (SWV) analysis was carried out within the potential range of −0.3 to 0.7 V at an amplitude of 0.01 V and frequency 15 Hz. Electrochemical impedance spectroscopy (EIS) analysis was carried out at an amplitude of 0.01 V within the frequency range of 100 KHz and 0.1 Hz.

2.3. Synthesis of the QDs

The synthesis of quinternary AuZnCeSeS QDs have previously been reported by Adegoke and coworkers [34]. Briefly, 1.2 g each of diethylzinc and cerium (IV) sulphate were mixed with 3 mL hexadecyl amine-capped gold nanoparticles, 15 mL oleic acid, 25 mL octadecene, 0.6 g myristic acid, 0.6 g HDA, 2 mL TOP and 1.8 g TOPO. The mixture was refluxed and stirred vigorously under heat in a 3-necked flask. Once

the reaction temperature reached ~260 °C, the Se precursor (3 mL), prepared by dissolving 0.12 g of Se in 5 mL TOP was added into the reaction mixture followed swiftly by the addition of the sulphur precursor (prepared by dissolving 0.16 g of sulphur with 5 mL oleic acid, 10 mL octadecene, 1 mL TOP and 0.9 g TOPO). The hydrophobic AuZnCeSeS QDs were allowed to grow for ~25 min (min) and were purified using a combination of acetone, ethanol and chloroform via ultracentrifugation.

2.4. Surface modification of the QDs

Prior to the encapsulation of the QDs with SiO_2, the QDs was first capped with 3-mercaptopropionic acid via a ligand exchange reaction. Briefly, the hydrophobic AuZnCeSeS QDs was dissolved in chloroform and added into a mixture of 3 mL 3-mercaptopropionic acid, 3 g potassium hydroxide and 40 mL methanol. The mixture was stirred vigorously for a few minutes and purified using acetone via ultracentrifugation. SiO_2 encapsulation of the QDs was carried out by mixing the 3-mercaptopropionic acid-AuZnCeSeS QDs (37 mg) in 20 mL methanol with 2 mL NH_3·OH, 5 mL TEOS, and 4 mL APTES. The mixture was stirred vigorously for 15 min at room temperature and purified using a combination of ethanol, acetone and chloroform via ultracentrifugation.

2.5. Electropolymerization reaction

For the fabrication of the sensing electrodes, the SPCEs were placed in a Petri dish and cleaned by sonicating first in Milli-Q H_2O, decanting the water, sonicating in 0.1 M HCl, decanting the acid solution and finally drying the surface with N_2 gas. CV was then used to further clean the SPCEs by sweeping in 0.1 M HCl within the potential range of −1.0 to +1.0 V (10 scans). Alternatively, the SPCEs were cleaned by sweeping in 0.5 M H_2SO_4 for 10 scans within the potential range of −1.5 to +1.5 V. Modification of the SPCE was carried out by drop-casting 6 μL of the QDs solution (1 mg/mL) prepared in 1 M Tris-HCl onto the pre-cleaned working electrode surface of the SPCE. The QDs/SPCE was then placed in the oven and dried at 70 °C. Once dried, the QDs/SPCE was washed with Milli-Q water and dried with N_2 gas. On the QDs/SPCE surface, 5 μL acrylamide (0.5 M in Milli-Q H_2O), 2 μL EGDMA (2 mM in H_2O:DMSO (2:1, v/v)), 2 μL AIBN (0.7 mM in H_2O:DMSO (1:1, v/v)), 2 μL $NaNO_3$ (0.3 M in Milli-Q H_2O) and 10 μL DZP (1000 μM in H_2O: ethanol (1:1, v/v)) was added and electropolymerization via CV was carried out within the potential range of −1.3 to +1.3 V at a scan rate of 0.05 V/s (10 scans). After the electropolymerization process, the MIP@QDs/SPCE was dipped in acetic acid:methanol (1:1, v/v) elution solution for 4 min to elute the template DZP. After elution of DZP, the MIP@QDs/SPCE was washed with Tris-HCl and dried with N_2 gas. To validate the MIP@QDs process, the non-imprinted polymer (NIP) reaction was carried out similarly to the MIP reaction except that the template DZP was not incorporated during the electropolymerization process.

2.6. DZP electrochemical assay

Under optimized reaction conditions, the detection of DZP was carried out by pipetting 2 μL DZP onto the MIP@QDs/SPCE surface and left to incubate for 2 min. After the incubation period, the MIP@QDs/SPCE was dried with N_2 gas. Thereafter, a solution of $K_3[Fe(CN)_6]/K_4[Fe(CN)_6]$-NaTKBor buffer was added onto the MIP@QDs/SPCE electrode surface. CV, SWV and EIS analysis were carried out as appropriate.

3. Results and discussion

3.1. Structural and optical characterization

Ligand exchange with MPA was first used to cap the QDs surface to stabilize the QDs surface and make the QDs biocompatible whilst the encapsulation in a silica layer was to introduce flexible silane networks on the QDs surface to make the QDs compact and more robustly solution-processable for MIP formation. The TEM surface morphological feature of the MPA-AuZnCeSeS QDs is presented in Fig. 1A. The observed morphology showed that the QDs were composed of quasi-spherical particles interlinked with each other. The relatively densely packed pattern of the QD particles is an indication of some degree of polydispersity and aggregation. Encapsulation of the MPA-AuZnCeSeS QDs in a silica shell changed the surface morphology of the particles as shown in the TEM image of SiO_2–AuZnCeSeS QDs (Fig. 1B). Individual quasi-spherical particles with a high degree of monodispersity were observed. The change in morphology of the particles is an indication of the robust salinization of the QDs surface. The average particle size of the QDs, as determined from the TEM images, was ~19 nm for MPA-AuZnCeSeS QDs and 69 nm for SiO_2–AuZnCeSeS QDs [34]. Fig. A1 and B1 shows the particle size distribution histogram for the MPA-AuZnCeSeS QDs and for SiO_2–AuZnCeSeS QDs. The increase in size after salinization was possibly due to the bulky nature of the silica particles.

SEM images of the bare SPCE, NIP@QDs/SPCE, MIP@QDs/SPCE (before elution) and MIP@QDs/SPCE (after elution) are shown in Fig. 1C–F. For the bare SPCE (Fig. 1C), the surface morphology was mainly composed of graphitic material-based carbon flakes. For the NIP@QDs/SPCE (Fig. 1D), the surface appeared very dense which is indicative of the polyacrylamide-EGDMA-AIBN film formation. However, for the MIP@QDs/SPCE (before elution) (Fig. 1E), the surface morphology appeared with uniform grains of polyacrylamide-EGDMA-AIBN film with the DZP template. Upon removal of the DZP template, the SEM image of the MIP@QDs/SPCE (after elution) (Fig. 1F), appeared rougher and porous with interconnected packed film.

EDX analysis was used to determine the elemental composition of the metal chalcogenide components of the QDs both quantitatively and qualitatively. Fig. 2A shows the EDX spectrum of the QDs with peaks for Au, Zn, Ce, Se and S clearly discernible. All metal chalcogenide components of the QDs were identified and quantified with Zn giving the highest elemental composition; (Au 1.14 %; Zn 44.10 %; Ce 0.97 %; Se 11.18 % and S 18.16 %).

The PXRD pattern of the SiO_2–AuZnCeSeS QDs is shown in Fig. 2B. The diffraction pattern was characterized by a strong single peak projected around 23° that can be ascribed to the plane {101}. As reported previously [34], the single peak is synonymous to amorphous silica and is an indication of the silica coating on the QDs surface.

UV/vis absorption and fluorescence emission spectra of the QDs measured in Tris-HCl solution are shown in Fig. 2C and D. From the UV/vis absorption spectrum of the QDs, a relatively weak excitonic peak was observed at 292 nm while the fluorescence emission was projected at a maximum wavelength of 530 nm. Since, no peak tailing was observed in the QDs, it is an indication of a suppressed deep trap state of the QDs surface, and this can be attributed to the robust synthesis used in the QDs fabrication.

To further characterize the photophysical properties of the QDs, the fluorescence quantum yield (QY) was determined according to equation (1):

$$\Phi_F^{QDs} = \Phi_F^{Rho} \frac{F_{QDs}.OD_{Rho\,(\lambda exc)}.n^2_{water}}{F_{Rho}.OD_{QDs\,(\lambda exc)}.n^2_{ethanol}} \quad (1)$$

Φ_F^{QDs} denotes the QDs fluorescence QY, Φ_F^{Rho} denotes the rhodamine 6G standard fluorescence QY ($\Phi = 0.95$) [35], F_{Rho} and F_{QDs} are the integrated sum of the fluorescence intensity of rhodamine 6G and the QDs, $OD_{QDs\,(\lambda exc)}$ and $OD_{Rho\,(\lambda exc)}$ are the optical densities of the QDs and rhodamine 6G while n^2_{water} and $n^2_{ethanol}$ are the square of the refractive indices of water used to dissolve the QDs and ethanol used to dissolve the standard. The calculated fluorescence QY for SiO_2–AuZnCeSeS QDs was 19 %.

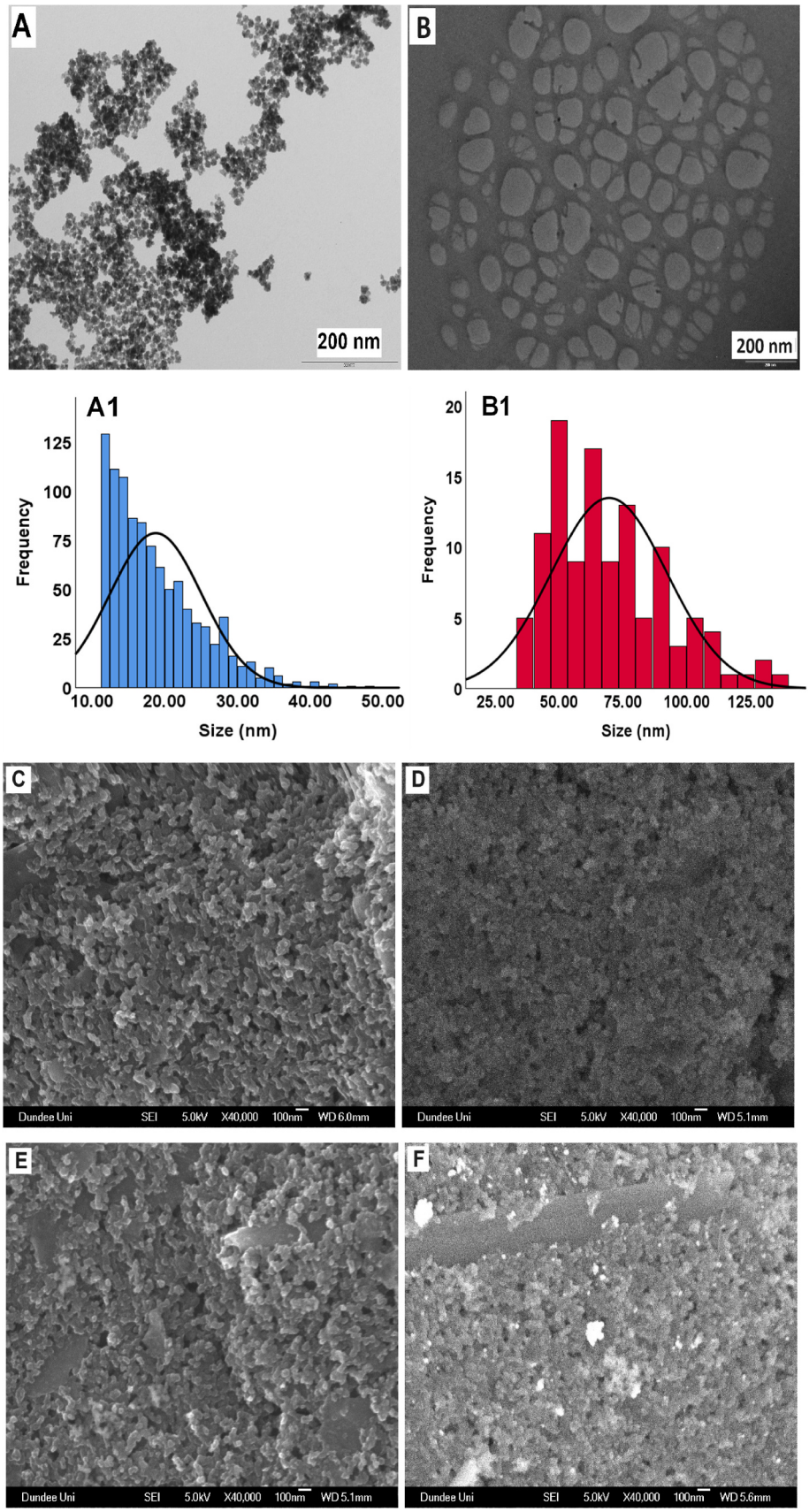

Fig. 1. TEM images and particle size histogram of (A and A1) MPA-AuZnCeSeS QDs and (B and B1) SiO_2-MPA-AuZnCeSeS QDs. SEM images of (C), bare SPCE, (D) NIP@QDs/SPCE, (E) MIP@QDs/SPCE (before elution) and (F) MIP@QDs/SPCE (after elution).

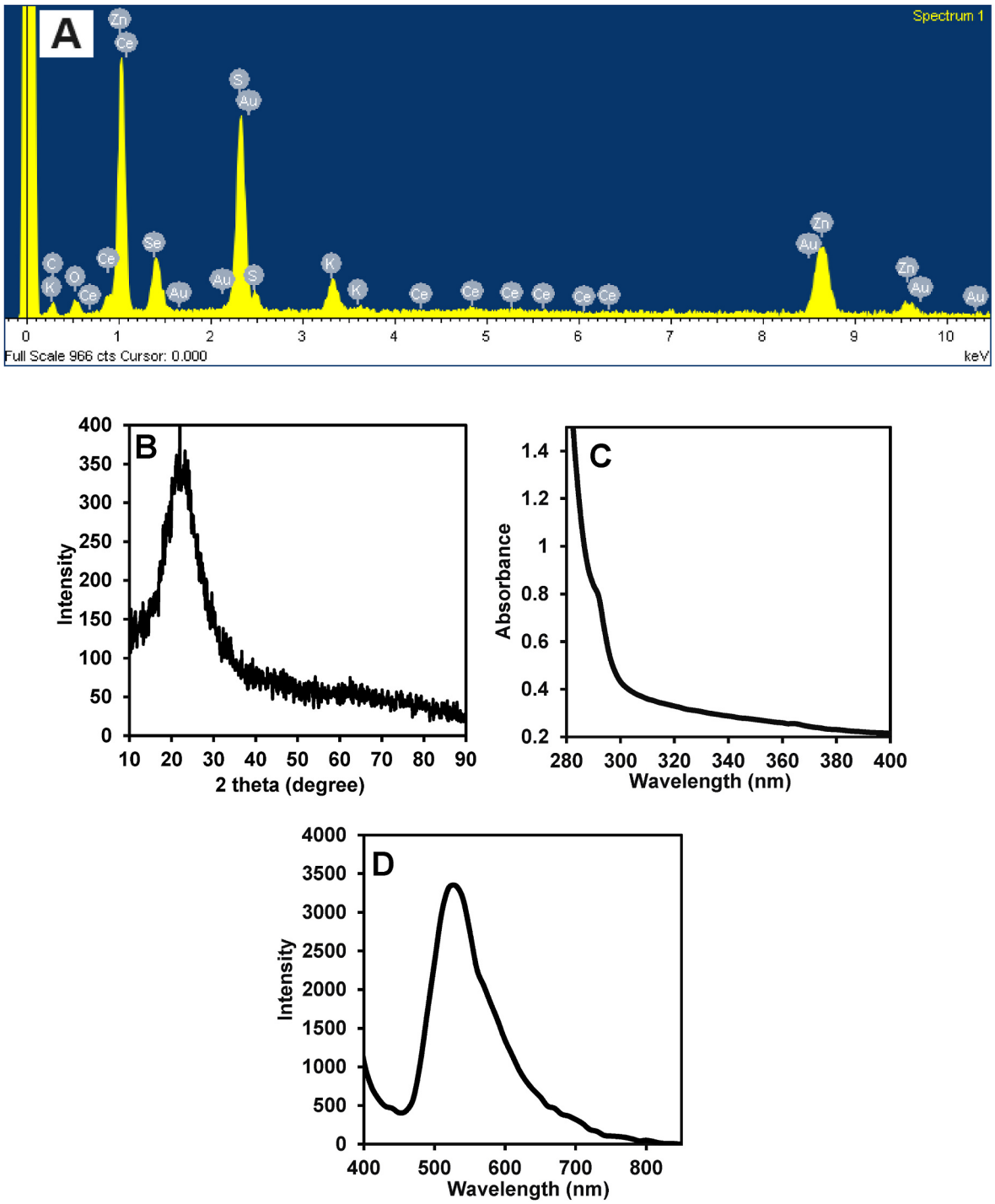

Fig. 2. (A) EDX spectrum, (B) PXRD, and (C) UV/vis absorption (E) and fluorescence emission (E) spectra of the SiO_2–AuZnCeSeS QDs.

3.2. Electrode surface characterization

CV was used to study the electron transfer properties and redox behaviour of chemical species at an electrode/electrolyte interface. The CV behaviour of the $K_3[Fe(CN)_6]/K_4[Fe(CN)_6]$ redox couple was used to study the electron transfer properties of the QDs/SPCE surface. Supporting electrolytes is essential in electrochemical studies to maintain the ionic strength of the electrolyte, enhance solution conductivity by increasing ion concentrations and preventing variations in the solution resistance [36] and electrode polarization. The supporting electrolytes can be inorganic salts, organic salts or buffer solutions, that are electrochemically inactive within the applied potential range. Buffer solutions are used in some electrochemical sensing systems to stabilize the pH, minimize electrode fouling and prevent fluctuations that could affect the sensor performance. Recently, we reported a new buffer system consisting of NH_4Ac, NaAc, KCl, KSCN, and Borax [37] denoted as NaTKBor buffer. To investigate the effect of NaTKBor buffer as a supporting electrolyte for the investigation of the $K_3[Fe(CN)_6]/K_4[Fe(CN)_6]$ redox process at the QDs/SPCE, its electrochemical behaviour was compared to that of phosphate buffer and phosphate buffer saline (PBS), used as supporting electrolytes for the CV experiments. Fig. 3A–S1A and S1B show the CV of the bare SPCE and QDs/SPCE in $K_3[Fe(CN)_6]/K_4[Fe(CN)_6]$-NaTKBor, $K_3[Fe(CN)_6]/K_4[Fe(CN)_6]$- PBS buffer and $K_3[Fe(CN)_6]/K_4[Fe(CN)_6]$-phosphate buffer. The change (Δ) in the anodic

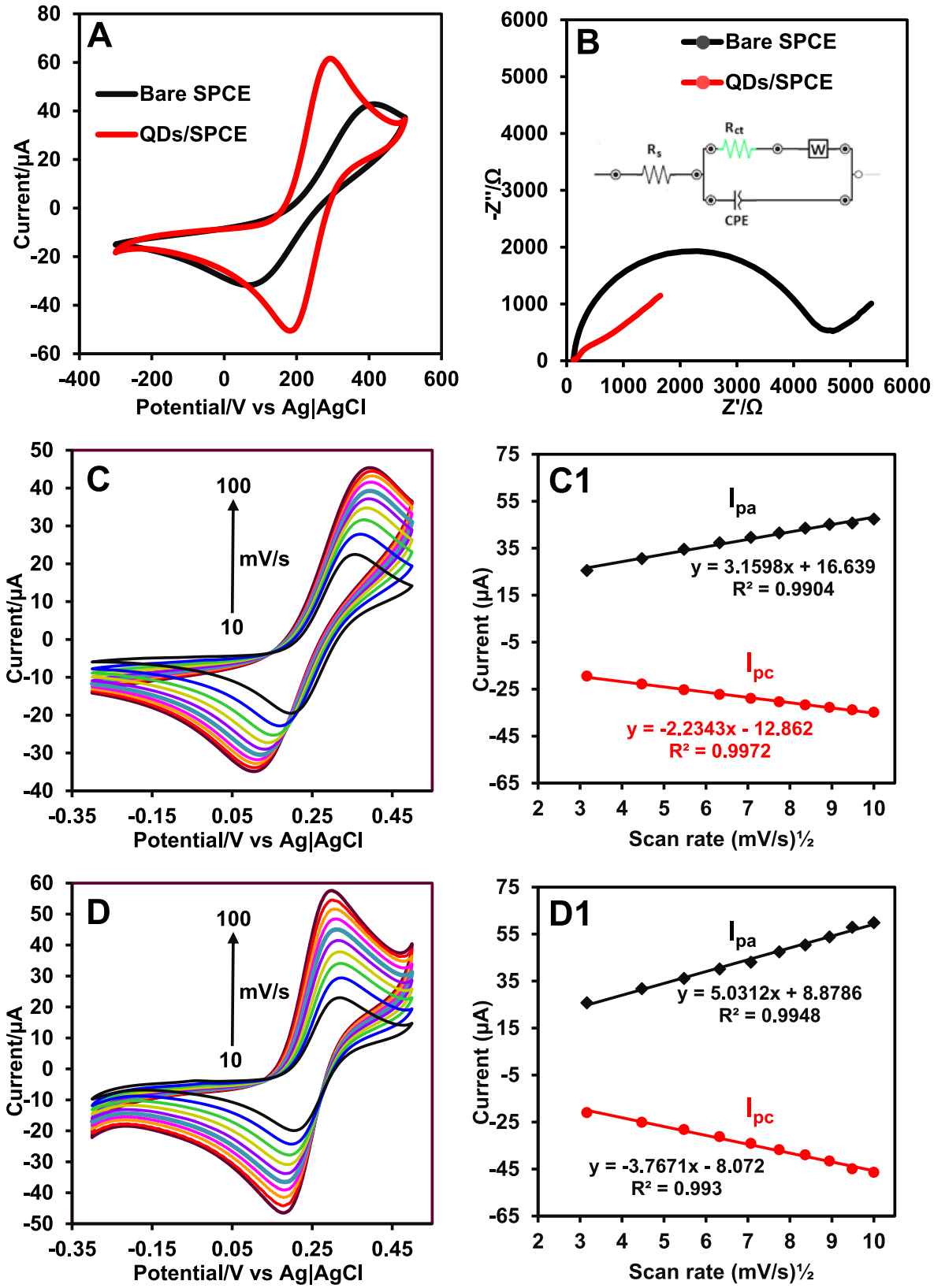

Fig. 3. (A) CV and (B) EIS plots of the bare SPCE and QDs/SPCE. Corresponding plots of the square root of the scan rate vs the I_{pa} and I_{pc} for the bare SPCE (C and C1) and QDs/SPCE (D and D1) in $K_3[Fe(CN)_6]/K_4[Fe(CN)_6]$-NaTKBor. 0.1 M KCl was used as a supporting electrolyte. Inset of Fig. 2B is the Randles equivalent circuit used to fit the EIS Nyquist plot.

peak current intensity, I_{pa} ($\Delta I_{pa} = I_{pa(QDs/SPCE)} - I_{pa(SPCE)}$) was higher in $K_3[Fe(CN)_6]/K_4[Fe(CN)_6]$-NaTKBor (22 μA) than $K_3[Fe(CN)_6]/K_4[Fe(CN)_6]$-PBS buffer (19 μA) and $K_3[Fe(CN)_6]/K_4[Fe(CN)_6]$-phosphate buffer (14 μA). The higher current intensity suggests that the redox behaviour of $K_3[Fe(CN)_6]/K_4[Fe(CN)_6]$ on the QDs/SPCE was influenced by the buffer constituent. To understand the observed trend, we determined the conductivity of the buffers, and the ionic conductivity was 8.42 mS for PBS buffer, 2.74 mS for phosphate buffer and 18.28 mS for NaTKBor buffer. The higher ionic conductivity of NaTKBor buffer indicates a higher concentration of mobile ions in the solution, which reduces the electromigration effect and facilitates faster ion migration towards the QDs/SPCE surface. This resulted in an enhanced redox process and higher peak currents, relative to the other buffer with lower conductivity. Thus, NaTKBor buffer was chosen as the supporting electrolyte for further studies.

The QDs/SPCE was characterized using the $K_3[Fe(CN)_6]/K_4[Fe(CN)_6]$-NaTKBor redox probe. The voltammogram of the bare SPCE in Fig. 3A, exhibited an anodic peak potential of 236 mV and a cathodic peak potential of 39 mV, resulting in a peak-to-peak separation (ΔE_p) of 300 mV. The anodic peak current (I_{pa}) intensity was 43 mV, and the cathodic peak current (I_{pc}) was −12 mV for the bare SPCE. However, the ΔE_p decreased to 103 mV and the anodic and cathodic peak current intensity increased to 65 mV and 54 mV, respectively after the modification of the SPCE with the QDs (QDs/SPCE). The decreases in ΔE_p and increase in the current intensities indicated the QDs increased the electroactive surface area of the SPCE and promoted an efficient electron transfer process.

Electrochemical impedance spectroscopy (EIS) analysis of the bare SPCE and the QDs/SPCE was carried out to further characterize the electrode surface. Fig. 3B shows the EIS Nyquist plot of the bare SPCE and the QDs/SPCE in the $K_3[Fe(CN)_6]/K_4[Fe(CN)_6]$-NaTKBor redox probe. The EIS data was fitted with Randles equivalent circuit consisting of a solution resistance (R_s) charge transfer resistance (R_{ct}), a constant phase element (CPE) and a Wurburg impedance (W) (Fig. 2B inset). The Nyquist plot of the bare SPCE showed a semicircle with its diameter fitted to an R_{ct} of 4148.0 Ω. However, the diameter of the semicircle and magnitude of the R_{ct} decreased to 30.1 Ω for the modified QDs/SPCE. The EIS results further confirmed that the QDs facilitated an efficient charge transfer process at the SPCE. The enhanced electron transfer properties and higher electroactive surface area suggested that the QDs/SPCE could serve as a suitable transducer interface for electrochemical sensing applications.

3.3. Effect of scan rates

Further electrochemical characterization of the QDs/SPCE was carried out using CV scan rate studies to investigate the electrochemical process at the electrode. Fig. 3C and D shows the effect of scan rate on the CV of the bare SPCE and QDs/SPCE. For both the SPCE and QDs/SPCE, the I_{pa} and I_{pc} increased with increasing CV scan rates from 10 to 100 mV/s. The corresponding plots of the square root of the scan rate vs the I_{pa} and I_{pc} intensities for the bare SPCE and QDs/SPCE are shown in Fig. 3C1 and D1. From the plots, the linearity of the current intensities with the scan rate implies that the electrochemical process for both the bare SPCE and QDs/SPCE is diffusion-controlled. The plot of the scan rate vs the current intensities was also carried out for the bare SPCE and the QDs/SPCE as shown in Figs. S2A and B. The results showed that the correlation coefficient generated from the I_{pa} and I_{pc} plots for the bare SPCE was low. The result clearly showed that a diffusion-controlled process was favoured. However, for the QDs/SPCE, the correlation coefficient generated from the I_{pa} and I_{pc} plots was high which indicate a surface adsorption process could also take place.

Subsequent analysis was conducted to determine the electroactive surface area of the bare SPCE and QDs/SPCE using the Randles-Ševčík equation (at 25°C) [38] as expressed in equation (1).

$$I_{pa} = (2.69 \times 10^5) n^{3/2} A C (D\nu)^{1/2} \quad (1)$$

where I_{pa} corresponds to the anodic peak current maximum (μA), n corresponds to the number of the electrons involved in the redox reaction, A is the electrode surface area (cm^2), C is the concentration of the redox probe (mol/cm^3), D is the diffusion coefficient (cm^2/s), ν is the scan rate (V/s) and the constant (2.69×10^5) has units $Cmol^{-1}V^{-1/2}$. The electroactive surface area was estimated as 5.35×10^{-3} cm^2 for the bare SPCE and 5.81×10^{-3} cm^2 for the QDs/SPCE. The result confirmed the QDs/SPCE had a higher electroactive surface area than the bare SPCE.

3.4. Electropolymerization

The QDs/SPCE was modified with an MIP layer via an electropolymerization process using CV. As detailed in the experimental section, an imprinting solution consisting of acrylamide as the monomer, EGDMA as the cross-linker, AIBN as an initiator, and DZP as the template was used for the electropolymerization. Fig. 4 shows the CV of the QDs/

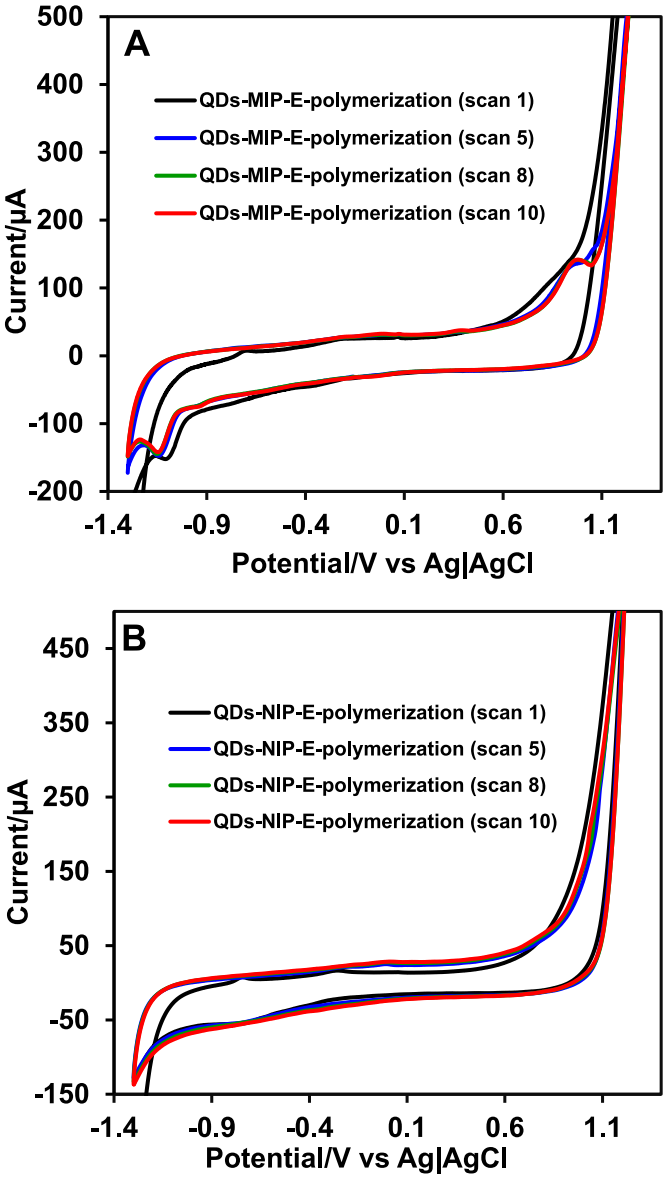

Fig. 4. CV of the MIP@QDs electropolymerization (A) and NIP@QDs electropolymerization (B) at scans 1, 5, 8 and 10.

SPCE in the imprinting solution conducted at a scan rate of 0.05 V/s for the 1st, 5th, 8th and 10th CV scans with the DZP template (Fig. 4A) for the fabrication of the MIP@QDs/SPCE and without the template (Fig. 4B) for the fabrication of NIP@QDs/SPCE. For the electropolymerization process of the MIP@QDs/SPCE formation, a cathodic reduction peak at −1.104. V with cathodic current at −152 μA was observed at scan 1. Subsequently, at scan 5, the cathodic potential has shifted to −1.143 V and the cathodic current had increased slightly to −148 μA. Also, an anodic oxidation peak was observed at 0.947 V with an anodic peak current of 0.133 μA. At scan 8 and scan 10, both the cathodic and anodic peaks were projected with no evidence of surface passivation. However, for the electropolymerization process of the NIP@QDs/SPCE formation, no apparent cathodic or anodic peak was seen. We believe, the presence of the DZP template during the electropolymerization process for the MIP@QDs/SPCE may have influenced the peak formation. The generally expected interaction during the MIP@QDs electropolymerization process is the binding interaction between the monomer and template.

3.5. MIP@QDs/SPCE characterization

Fig. 5A shows the comparison of the CV and EIS Nyquist plots for the (i) QDs/SPCE, (ii) MIP@QDs/SPCE (before elution), (iii) MIP@QDs/SPCE (after elution), (iv) MIP@QDs/SPCE (DZP rebind), (v) NIP@QDs/SPCE (before elution), (vi) NIP@QDs/SPCE (after elution) and NIP@QDs/SPCE (DZP rebind) in $K_3[Fe(CN)_6]/K_4[Fe(CN)_6]$-NaTKBor redox solution. Due to the lack of passivation of the QDs/SPCE from the electropolymerization process, there was an increase in I_{pa} and I_{pc} of the MIP@QDs/SPCE (before elution) and NIP@QDs/SPCE (before elution) relative to the QDs/SPCE. The current increase is indicative of increased surface area of the QDs/SPCE due to the polymer formation on the electrode surface. The decrease in I_{pa} and I_{pc} for the MIP@QDs/SPCE (before elution) relative to the NIP@QDs/SPCE (before elution), can be attributed to the presence of DZP during the electropolymerization process. The CVs showed well-resolved anodic and cathodic peaks due to the ferricyanide-ferrocyanide redox process for both the MIP@QDs/SPCE (after elution) and NIP@QDs/SPCE (after elution). However, for the MIP@QDs/SPCE (after elution), both the oxidation and reduction peaks were at a lower peak current relative to the NIP@QDs/SPCE (after elution) and this further proves the presence of DZP being imprinted on the polymer. The CV of the MIP@QDs/SPCE (DZP rebind) and NIP@QDs/SPCE (DZP rebind) both exhibited a decrease in the intensities of the oxidation and reduction peaks and higher ΔE_p values. The decreased peak current confirmed the rebinding of DZP into the created cavities of the MIP@QDs/SPCE. The slight increase in peak current for the NIP@QDs/SPCE (DZP rebind) relative to the MIP@QDs/SPCE (DZP rebind) may be due to the absence of created cavities.

The corresponding EIS Nyquist plots are shown in Fig. 5B. The Nyquist plot of the (i) QDs/SPCE, (ii) MIP@QDs/SPCE (before elution), (iii) MIP@QDs/SPCE (after elution), NIP@QDs/SPCE (before elution) and (vi) NIP@QDs/SPCE (after elution) did not show a semicircle, which confirms a low resistance to charge transfer. However, after the interaction with DZP, the Nyquist plot of the MIP@QDs/SPCE (DZP rebind) and NIP@QDs/SPCE (DZP rebind) showed a semicircle, indicating the binding of DZP inhibited the charge transfer process. Using the Randles equivalent circuit (inset of Fig. 5B) to fit the EIS data, an R_{ct} of 1939 Ω was obtained for the MIP@QDs/SPCE and R_{ct} of 1017 Ω was obtained for the NIP@QDs/SPCE. The higher R_{ct} for the MIP@QDs/SPCE relative to the NIP@QDs/SPCE is indicative of stronger interaction with DZP which may imply rebinding of the drug into the created cavities.

Fig. 5C shows the Bode impedance plots for the studied systems. The general observation was the increase in impedance for the (iv) MIP@QDs/SPCE (DZP rebind) and (vii) NIP@QDs/SPCE (DZP rebind) relative to the (i) QDs/SPCE and the other studied system in the low frequency region, i.e., between 0.1 and 150 Hz. The decrease in impedance which was more pronounced for the (ii) MIP@QDs/SPCE (before elution) and (v) NIP@QDs/SPCE (before elution) across the entire frequency region, implies that both systems tend towards capacitive behaviour. The increased impedance of the (iv) MIP@QDs/SPCE (DZP rebind) relative to the (vii) NIP@QDs/SPCE (DZP rebind) is due to the higher resistive behaviour of the former arising from the DZP binding to the created cavities.

From the Bode phase plots shown in Fig. 5D, a systematic phase shift at lower frequencies was observed for the (ii) MIP@QDs/SPCE (before elution) (−54.7° at 0.52 Hz) and (v) NIP@QDs/SPCE (before elution) (−55.2° at 0.41 Hz) relative to the (i) QDs/SPCE (−33.2° at 6.8 Hz). However, a phase shift at much higher frequencies was observed for the (iv) MIP@QDs/SPCE (DZP rebind) (50.3° at 44.1 Hz) and (vii) NIP@QDs/SPCE (DZP rebind) (36.8° at 17.3 Hz). We observed a significant distinction between the phase shift for the MIP@QDs/SPCE (DZP rebind) and the NIP@QDs/SPCE (DZP rebind). The increase in phase angle at increased frequency for the MIP@QDs/SPCE (DZP rebind) is indicative of decreased impedance of the resistive component of the dielectric. Whereas, the higher phase angle at lower frequency for the other systems, is indicative of a system than tends to behave as a pseudo capacitor since a phase angle close to −90°, represents a capacitive type of system.

Square wave voltammetry (SWV) analysis was also used to confirm the rebinding of DZP to the MIP@QDs/SPCE. Fig. 5E shows the comparative SWV of the MIP@QDs/SPCE (no DZP), MIP@QDs/SPCE (DZP rebind), NIP@QDs/SPCE (no DZP) and QDs-NIP/SPCE (DZP rebind) measured in $K_3[Fe(CN)_6]/K_4[Fe(CN)_6]$-NaTKBor redox probe. From the displayed data, the ΔI_{pa} (I_{pa} of MIP@QDs (no DZP) - I_{pa} of MIP@QDs (DZP rebind)) was significantly higher than the ΔI_{pa} (I_{pa} of NIP@QDs (no DZP) - I_{pa} of NIP@QDs (DZP rebind)) and thus confirms the rebinding of DZP to the created cavities of the MIP@QDs/SPCE.

3.6. Optimization of sensor fabrication step and DZP assay parameters

The effect of cycle number, elution time and incubation time were investigated using EIS and SWV. Fig. 6A - C shows the Nyquist plots for the effects of cycle number, elution time and incubation time of the MIP@QDs/SPCE in the $K_3[Fe(CN)_6]/K_4[Fe(CN)_6]$-NaTKBor redox probe. The diameter of the semicircle was indicative of the magnitude of R_{ct}. Fig. 6A1 – C1 shows the corresponding plots of the cycle number, elution time and incubation time versus (vs) the R_{ct} whilst Figs. S3A–C shows the plots of the cycle number, elution time and incubation time vs the ΔI_{pa} (ΔI_{pa} = I_{pa} MIP@QDs/SPCE (no DZP) - I_{pa} MIP@QDs/SPCE (with DZP) obtained from SWV. For the EIS analysis, the highest R_{ct} value was chosen as an optimum sensor signal. Fig. 6A1 and S3A showed that the optimum nanosensor signal was obtained at 10 CV cycles for the electropolymerization process. Thus, 10 cycles were chosen as the optimum number of CV cycles for the MIP@QDs/SPCE fabrication. For the effect of elution time, Fig. 6B1 and S3B confirmed that the highest signal response was obtained after 4 min of elution time. Hence, 4 min was chosen as the optimum DZP elution time for the nanosensor fabrication. Lastly, the effect of incubation time used during the assay was optimized. The R_{ct} (Fig. 6C1) and ΔI_{pa} (Fig. S3C) obtained showed that the optimum incubation time for DZP determination was at 2 min and this time was chosen for the assay. Fig. 6D shows the Randles equivalent circuit used to fit the EIS Nyquist plots for the effect of cycle number whilst Fig. 6E shows the Randles equivalent circuit used to fit the EIS Nyquist plots of elution time and incubation time. Generally, the results showed that EIS and SWV data were complementary and could successfully be used in tandem for the electrochemical determination of DZP.

3.7. Assay selectivity, reusability, reproducibility/stability

Assay selectivity for DZP detection using the developed MIP@QDs/SPCE electrochemical nanosensor was investigated with EIS. All the non-targeted benzodiazepine drugs were tested under the same experimental

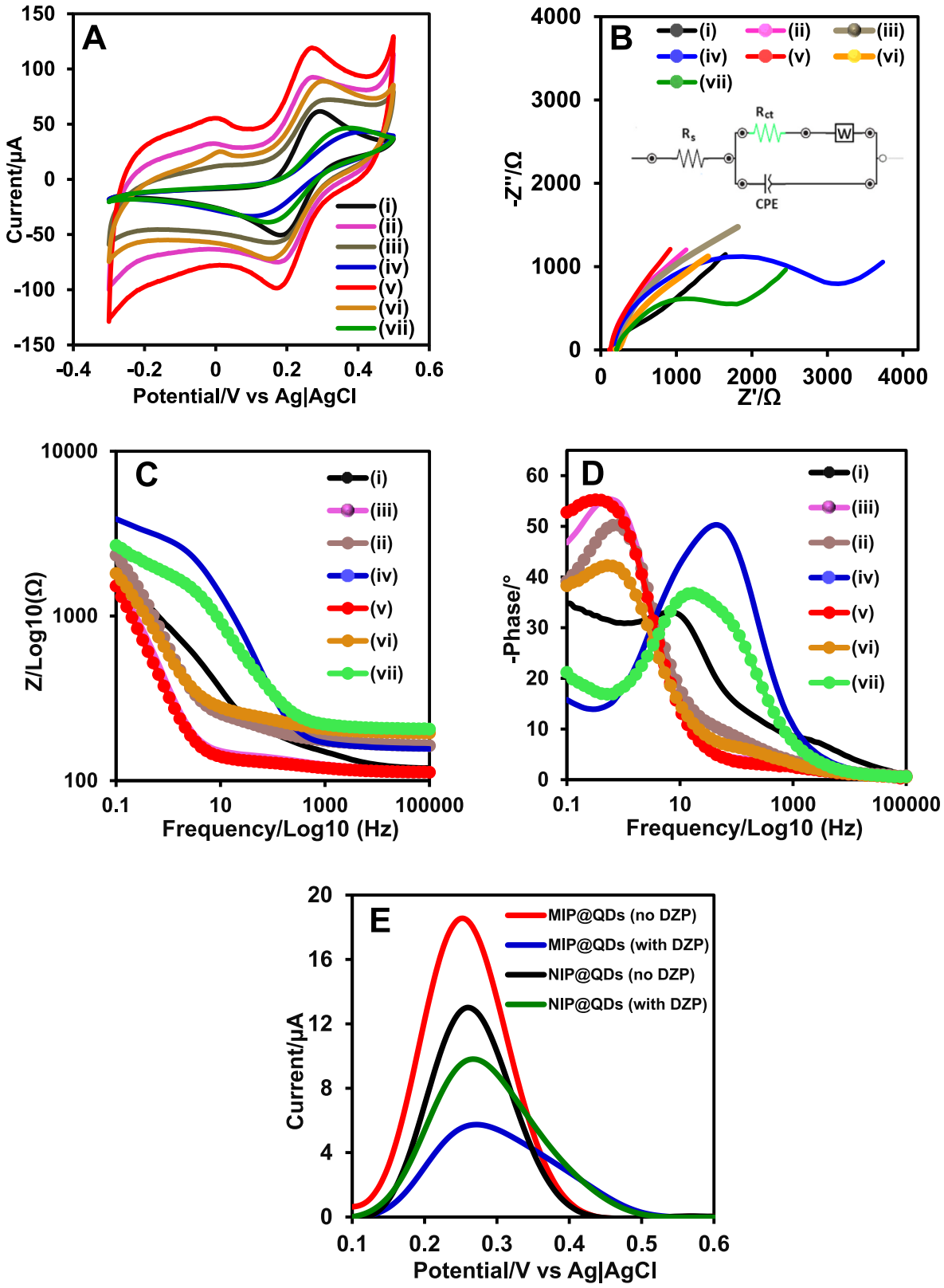

Fig. 5. (A) CV, (B) EIS Nyquist plots and (C) Bode impedance and (D) Bode phase of the (i) QDs/SPCE, (ii) MIP@QDs/SPCE (before elution), (iii) MIP@QDs/SPCE (after elution), (iv) MIP@QDs/SPCE (DZP rebind), (v) NIP@QDs/SPCE (before elution), (vi) NIP@QDs/SPCE (after elution) and (vii) NIP@QDs/SPCE (DZP rebind). (E) SWV of the MIP@QDs/SPCE (no DZP), MIP@QDs/SPCE (with DZP), NIP@QDs/SPCE (no DZP) and NIP@QDs/SPCE (with DZP) in $K_3[Fe(CN)_6]/K_4[Fe(CN)_6]$-NaTKBor. 0.1 M KCl was used as a supporting electrolyte. Inset of Fig. 4B: Randles equivalent circuit used to fit the QDs@ MIP (with DZP) and QDs@ NIP (with DZP).

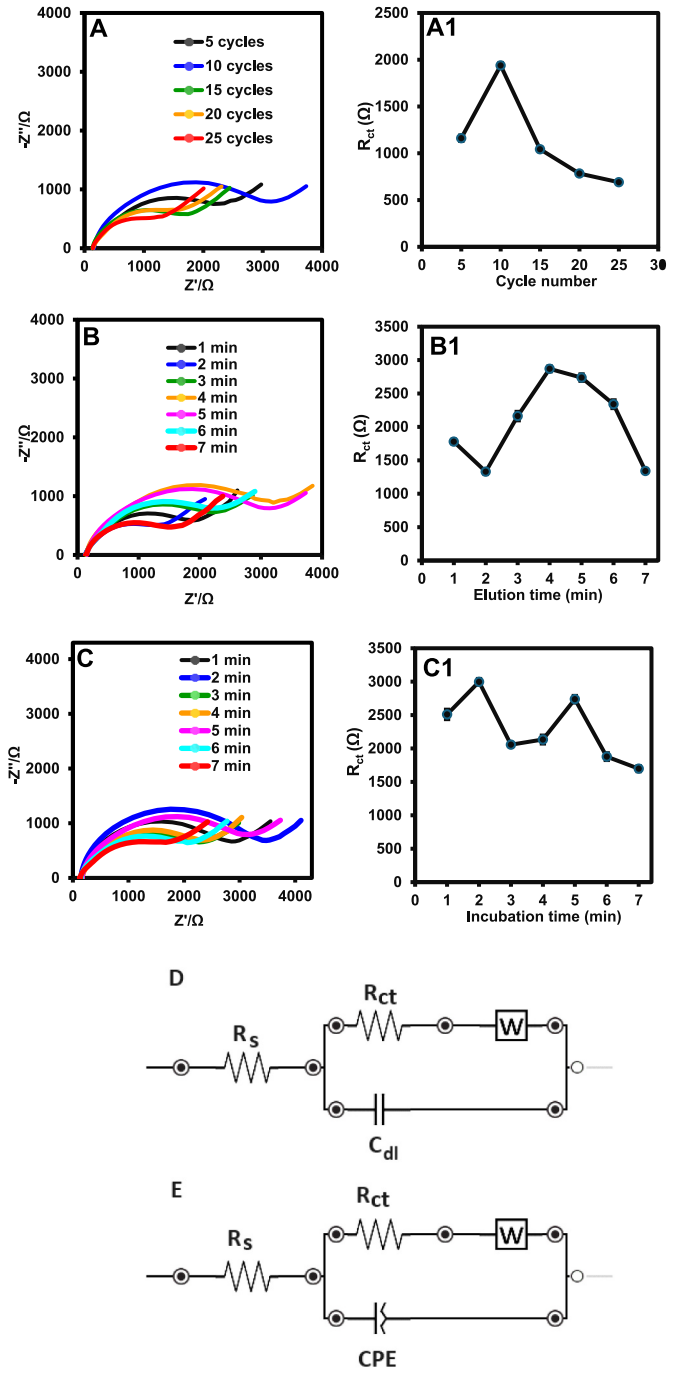

Fig. 6. EIS Nyquist plots of the effect of (A) cycle number, (B) elution time and (C) incubation time using the MIP@QDs/SPCE. Corresponding plot of the effect of (A1) cycle number, (B1) elution time and (C1) incubation time vs the generated R_{ct}. Randles equivalent circuit used to fit the EIS Nyquist plots for the effect of (D) cycle number and (E) elution time and incubation time. $K_3[Fe(CN)_6]/K_4[Fe(CN)_6]$-NaTKBor was used as the redox probe/electrolyte solution. C_{dl} = double layer capacitance.

conditions as the target DZP. Fig. 7A shows the EIS Nyquist plots for DZP detection in comparison to other tested benzodiazepine drugs using the MIP@QDs/SPCE whilst Fig. 7B shows the EIS Nyquist plots for tested benzodiazepine drugs using the NIP@QDs/SPCE. From the results, it showed clearly that the MIP@QDs/SPCE nanosensor was more selective to DZP than other non-targeted drugs as judged by the magnitude of the semicircle whilst the NIP@QDs/SPCE did not exhibit selectivity for DZP. The corresponding R_{ct} response shown in Fig. 7C, clearly confirmed the selectivity of the MIP@QDs/SPCE nanosensor for DZP based on the higher R_{ct} value obtained compared to the values obtained for other tested benzodiazepines whist the R_{ct} response from the NIP@QDs/SPCE did not show any selectivity for DZP.

The reusability of the MIP@QDs/SPCE nanosensor towards DZP detection was investigated. Fig. 7D shows the R_{ct} response for DZP detection across 5 repetitive measurements on the same MIP@QDs/SPCE whilst Fig. S4A shows the corresponding EIS Nyquist plots. The results showed that the MIP@QDs/SPCE nanosensor can be reused several times without loss of current signal as the RSD obtained from five repetitive measurements was 2.4 %. The reproducibility/stability of the MIP@QDs/SPCE nanosensor across difference electrodes was also investigated. Fig. 7E shows the R_{ct} response for DZP detection across five different MIP@QDs/SPCE's and Fig. S4B shows the corresponding EIS Nyquist plots. The results showed that sensor-to-sensor variability across different electrodes was marginally acceptable as the RSD obtained was 11.4 %. Based on this results, the sensor showed high sensor-to-sensor reusability and reproducibility.

3.8. Quantitative DZP detection

Quantitative detection of DZP was carried out using the MIP@QDs/SPCE detection system in the $K_3[Fe(CN)_6]/K_4[Fe(CN)_6]$-NaTKBor redox probe on a portable hand-held Palmsens 4 potentiostat connected via Bluetooth to a laptop computer. Fig. 8A shows the EIS Nyquist plots for the quantitative detection of DZP within the concentration range of 0.1–100 μM using the MIP@QDs/SPCE. The Nyquist plot of the baseline signal (without DZP) did not show a semicircle, implying low R_{ct}. However, as DZP concentrations increased in the system, the semicircle diameter increased due to the binding of more DZP molecules onto the MIP@QDs/SPCE. The binding of the DZP molecules inhibited the charge transfer process resulting in higher R_{ct}. These results generally showed that as the concentration of DZP increased, the R_{ct} also increased. The corresponding calibration plot shown in Fig. 8A1 was linear within the range of 0.1–100 μM for DZP using the MIP@QDs/SPCE. Using three times the standard deviation of blank measurements divided by the slope of the calibration plot, the limit of detection (LOD) was calculated as 4.9 μM for DZP using the MIP@QDs/SPCE. To confirm the validity of the MIP@QDs/SPCE for DZP quantitative detection, the NIP@QDs/SPCE was also quantitatively used in the detection of DZP. As shown in Fig. 8A1, the NIP@QDs/SPCE did not quantitatively detect DZP, thus validating the MIP@QDs/SPCE as an efficient electrochemical nanosensor for DZP detection.

3.9. Detection in saliva

Quantitative detection of DZP in saliva was carried out using the MIP@QDs/SPCE in the $K_3[Fe(CN)_6]/K_4[Fe(CN)_6]$-NaTKBor redox probe to demonstrate detection in a complex biological sample on (i) a portable potentiostat connected to a laptop computer and (ii) on a hand-held potentiostat connected to a smartphone device. Untreated saliva was collected ethically and spiked with a known concentration of DZP in a 1:1 ratio.

Use of a portable potentiostat connected to a laptop computer: Fig. 8B shows the EIS Nyquist plots for the quantitative detection of DZP in saliva within the concentration range of 0.1–100 μM on the portable potentiostat and Fig. 8B1 shows the corresponding calibration plot. The shape of the EIS Nyquist plots lacked the presence of Warburg resistance suggesting the absence of ion diffusion at the interface between the electrode and electrolyte. The calculated LOD was 2.3 μM for DZP determination in saliva using the portable potentiostat.

Use of a hand-held potentiostat connected to a smartphone device: Fig. 8C shows the EIS Nyquist plot obtained for DZP quantitative detection within the concentration range of 1–1000 μM on the hand-held potentiostat connected to a smartphone device and Fig. 8C1 shows the calibration plot. The result revealed that rebinding of DZP on

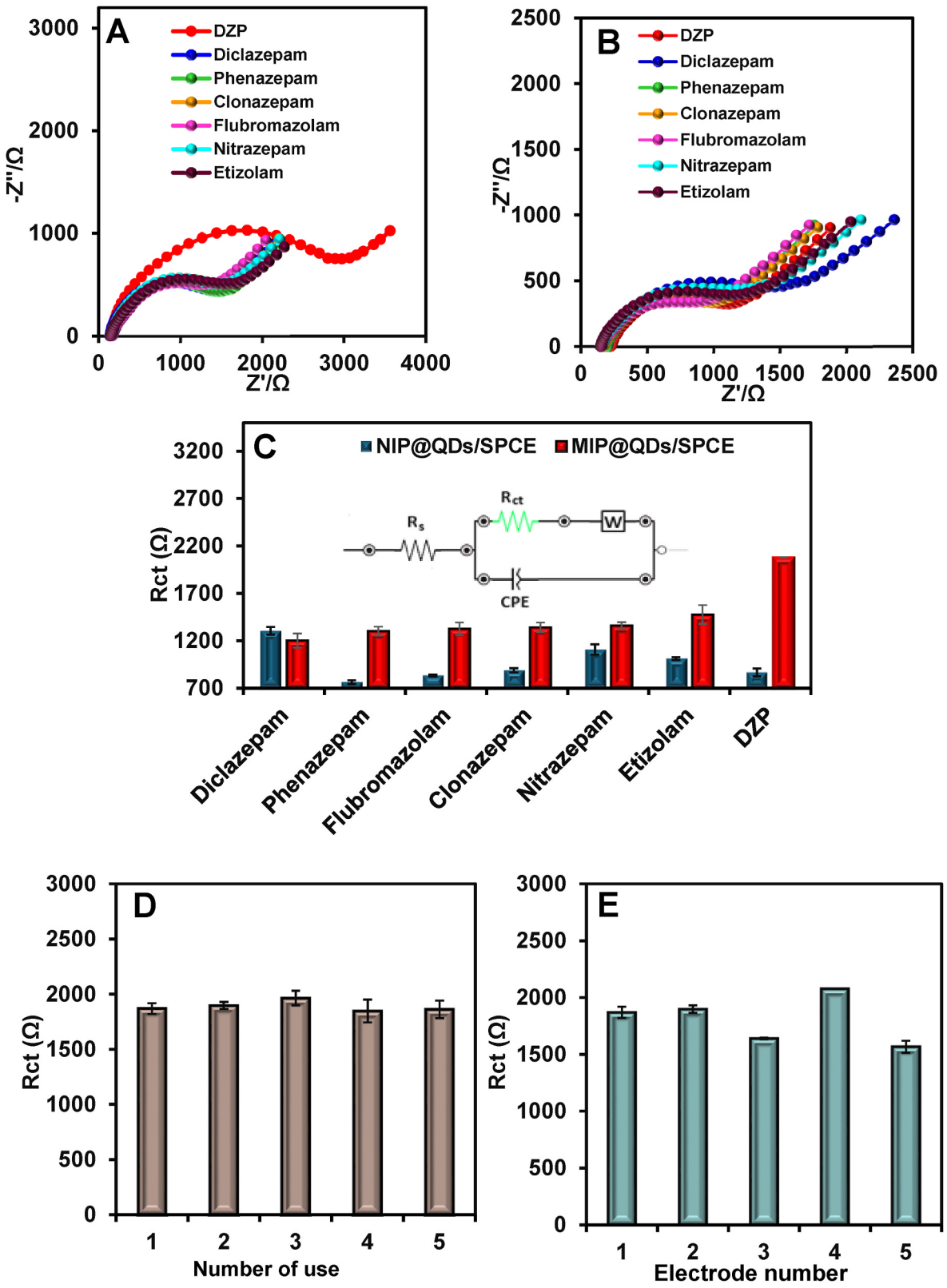

Fig. 7. EIS Nyquist plots showing the selectivity of the (A) MIP@QDs/SPCE and (B) NIP@QDs/SPCE towards DZP and other non-targeted benzodiazepines. (C) Corresponding R_{ct} response showing the selectivity of the MIP@QDs/SPCE and NIP@QDs/SPCE towards DZP detection in comparison to other non-targeted benzodiazepine drugs. R_{ct} response showing the (D) repeatability and (E) reproducibility/stability of the MIP@QDs/SPCE nanosensor. [DZP] and other drugs = 100 μM. Inset of Fig. 6C: Randles equivalent circuit used to fit the EIS Nyquist plots shown in Fig. 6B.

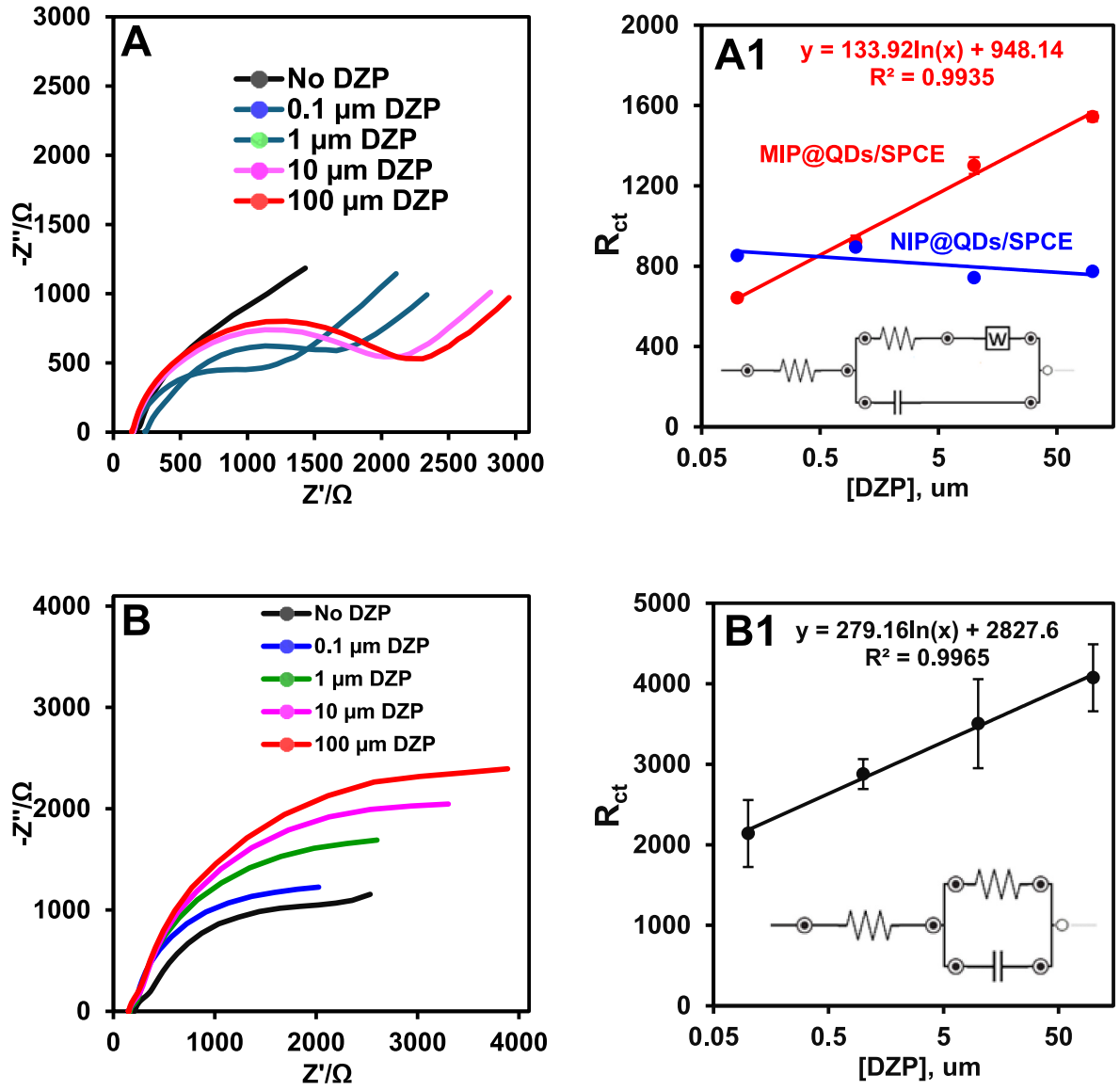

Fig. 8. EIS Nyquist plots for the quantitative detection of DZP in ethanol:H_2O (A) and saliva (B) on a portable potentiostat connected to a laptop computer and the detection of DZP in saliva (C) on a hand-held smartphone-based potentiostat using the MIP@QDs/SPCE nanosensor. Calibration plots for DZP quantitative detection showing DZP concentrations vs the generated R_{ct} in (A1) ethanol:H_2O, (B1) saliva with a portable potentiostat used and (C1) saliva with a hand-held smartphone-based potentiostat used. (D) SWV for the quantitative detection of DZP and the (D1) corresponding calibration plots for DZP quantitative detection using the MIP@QDs/SPCE nanosensor. For Fig. 8D1: ΔI = MIP@QDs/SPCE (no DZP) - MIP@QDs/SPCE (with DZP). Inset of Fig. 8A1, B1 and C1 = Randles equivalent circuit used to fit the EIS Nyquist plot. Control for Fig. 8B and C = MIP@QDs/SPCE (saliva with no spiked DZP).

the MIP@QDs/SPCE led to simultaneous increase in the generated R_{ct} as the concentration of DZP increased in the system. The calculated LOD was 2.7 µM which is relatively higher than the LOD obtained using the portable potentiostat. In terms of cost, the smartphone potentiostat (Sensit Smart) is four times much cheaper than the portable potentiostat (Palmsens 4), making it a more affordable system. However, the Palmsens 4 is a much faster potentiostat (~3 min for 50 frequencies) to run EIS than the smartphone-based Sensit Smart potentiostat (~20 min for 50 frequencies). In general, our developed MIP@QDs/SPCE nanosensor system demonstrates the potential for point-of-use with the trade-off between sensitivity, cost and response time with regard to the choice of portable potentiostat.

3.10. Voltammetric DZP detection

Voltammetric DZP detection using the developed MIP@QDs/SPCE nanosensor was carried out in the $K_3[Fe(CN)_6]/K_4[Fe(CN)_6]$-NaTKBor redox probe to demonstrate the robustness of our assay system to be analysed by another electrochemical technique. Fig. 8D shows the SWV obtained for DZP quantitative detection within the concentration range of 0.1–1000 µM. The result showed that rebinding of DZP on the MIP@QDs/SPCE led to simultaneous decrease of the I_{pa}. The corresponding calibration plot of DZP concentration vs the ΔI_{pa} was linear (Fig. 8D1) and the calculated LOD was 1.0 µM and was lower than the LOD obtained using EIS technique. Table 1 shows that the LOD of the developed MIP@AuZnCeSeS QDs/SPCE nanosensor for DZP in comparison to other developed methods, offered improvement in sensitivity.

3.11. Reaction mechanism

Scheme 1A shows the descriptive fabrication of the MIP@QDs/SPCE electrochemical nanosensor for DZP. Firstly, organic-phased AuZnCeSeS

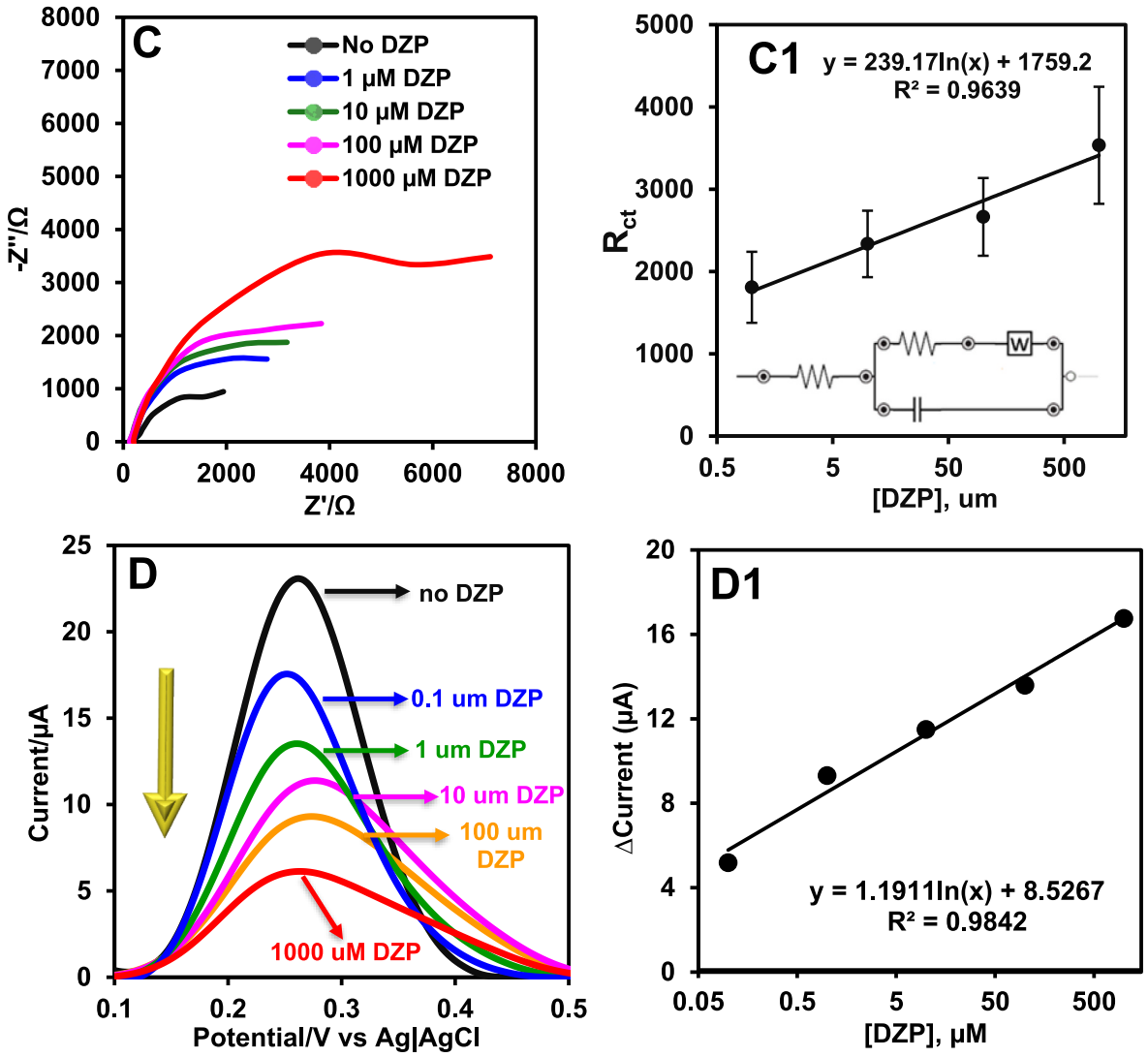

Fig. 8. (*continued*).

Table 1
Analytical performance of the developed MIP@AuZnCeSeS QDs/SPCE nanosensor for DZP in comparison to other developed probe.

Probe	Transduction technique	Linear range	LOD (μM)	Ref.
GS-MS	Chromatography	50–1000 μg/mL	30.6	[12]
Multipumping flow system	Fluorescence	–	5.2	[39]
Capillary Electrophoresis	Capillary electrophoresis-diode array detection	17.0–90.9 mg/mL	10.5	[15]
Unmodified SPCE	Adsorptive stripping voltammetry	7.1–285 μg/mL	6.3	[8]
Multiwall carbon nanotube-ionic liquid modified-SPE	SWV	24.9–1000	6.6	[40]
MIP@AuZnCeSeS QDs/ SPCE	EIS SWV	0.1–100 μM 0.1–1000 μM	2.3 1.0	**This Work**

QDs were synthesized and thereafter made water-soluble and compatible via a ligand exchange reaction with MPA. The QDs were thereafter encapsulated in silica and drop-casted onto SPCEs. Electropolymerization using CV was carried out to imprint the target DZP; thus, leading to the formation of the MIP@QDs/SPCE electrochemical detection system. DZP was eluted from the MIP@QDs/SPCE, leaving cavities of specific size and shape. Rebinding of DZP into the created cavities of the MIP@QDs/SPCE formed the basis for the detection of DZP. The QDs served as the interface to improve the electroactive surface area to induce higher sensitivity, the MIP served as the receptor to induce selective DZP recognition and $K_3[Fe(CN)_6]/K_4[Fe(CN)_6]$-NaTK-Bor served as the redox probe.

Scheme 1B provides a general interpretation of the electrochemical process. The general interpretation of the electrochemical process in the presence of the redox probe as shown in Scheme 1B, implies that at a negative applied potential, a reduction reaction occurs and electron from the QDs valence band is transferred to $[Fe(CN)_6]^{3-}$ leading to the formation of $[Fe(CN)_6]^{4-}$. Conversely, at a positive applied potential, an oxidation reaction occurs, and an electron from $[Fe(CN)_6]^{4-}$ is transferred to the conduction band of the QDs, leading to the formation of $[Fe(CN)_6]^{3-}$. However, when DZP binds to the MIP cavities, the DZP molecules passivate the MIP@QDs interface and disrupt the electronic transport between the QDs interface and the ferricyanide/ferrocyanide redox probe. This resulted in a decrease in the peak current in the SWV and increasing charge transfer resistance in the EIS signal as the DZP binds to the MIP@QDs/SPCE.

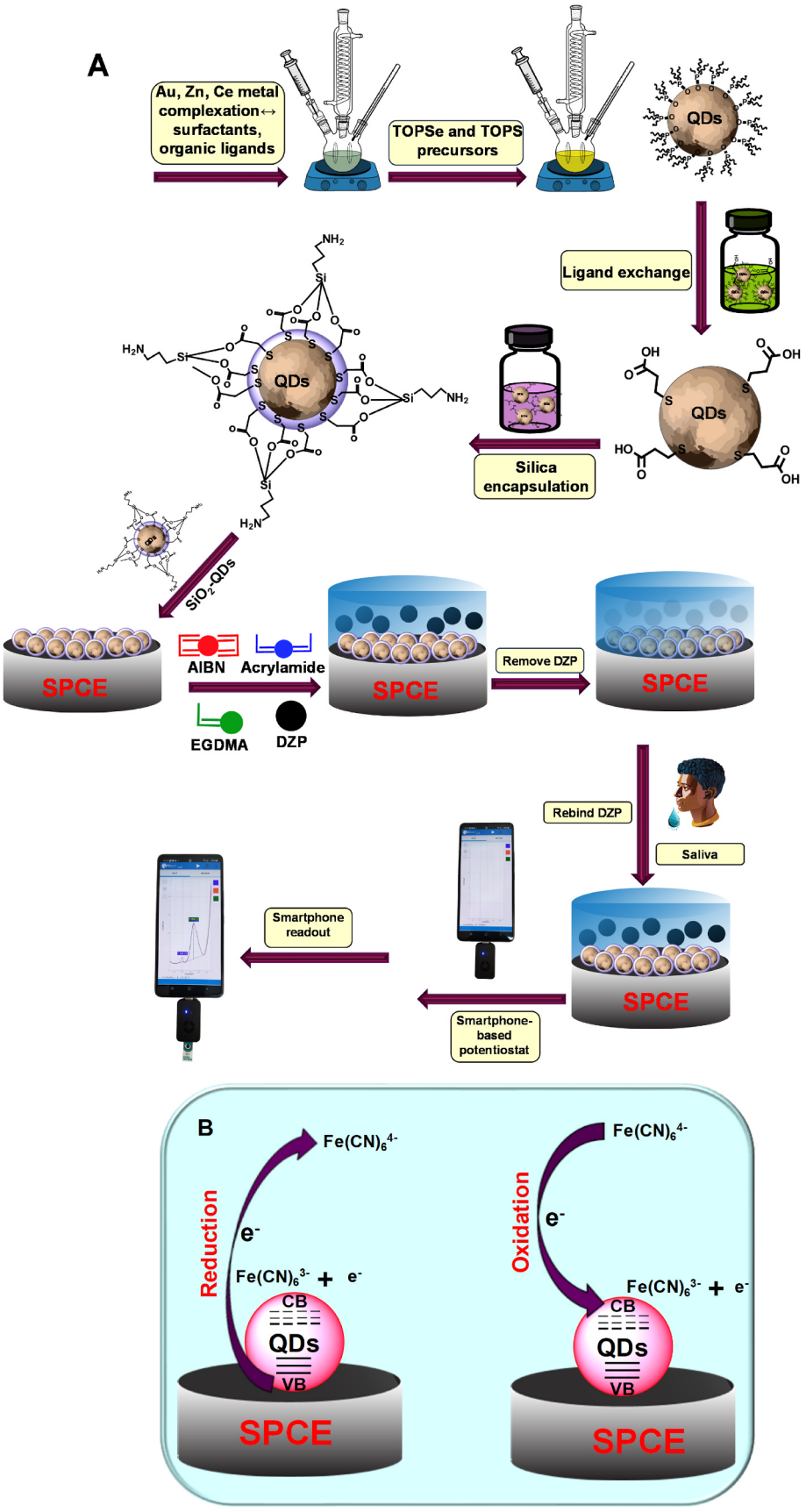

(caption on next page)

Scheme 1. Schematic representation of the electrochemical detection process for DZP using the MIP@QDs/SPCE nanoprobe. (A) The QDs were synthesized using the organometallic synthetic route and a ligand exchange reaction is used to coat the QDs surface with MPA. Silica encapsulation of the QDs is performed and the QDs are drop-casted on a SPCE. Electropolymerization using CV is carried out on the QDs/SPCE in the presence of acrylamide, EGDMA, AIBN, $NaNO_3$ and the template DZP. Using a Sensit Smart potentiostat connected to a smartphone, the MIP@QDs/SPCE without the template produces a high anodic peak current from the SWV but rebinding of DZP leads to decreased anodic peak current. Also, using a portable hand-held potentiostat with Bluetooth configuration to a computer, DZP was detected using EIS. (B) Schematic description of the electron transfer processes in the presence of the $K_3[Fe(CN)_6]/K_4[Fe(CN)_6]$ redox probe involving reduction and oxidation reactions.

4. Conclusion

A novel MIP@AuZnCeSeS QDs/SPCE electrochemical nanosensor has been successfully developed for DZP. Silica-encapsulated AuZnCeSeS QDs were drop-casted onto SPCEs and electropolymerization using CV was carried out on the QDs/SPCE in the presence of a functional monomer, cross linker, initiator and the target DZP. Using EIS as the electrochemical technique, DZP was detected quantitatively in ethanol:H_2O and in saliva via a portable potentiostat connected to a laptop and a hand-held smartphone potentiostat. The versatility of the MIP@QDs/SPCE electrochemical nanosensor for DZP detection was also demonstrated using SWV. This sensing platform may pave the way for the rapid detection of a spectrum of viral pathogens for medical diagnostic and environmental monitoring.

CRediT authorship contribution statement

Oluwasesan Adegoke: Writing – original draft, Project administration, Methodology, Investigation, Funding acquisition, Formal analysis, Data curation, Conceptualization. **Kayode Oyinlola:** Writing – review & editing, Formal analysis. **Kayode Omotayo Adeniyi:** Writing – review & editing, Formal analysis. **Ojodomo J. Achadu:** Writing – review & editing. **Zhugen Yang:** Writing – review & editing. **Niamh Nic Daeid:** Writing – review & editing, Funding acquisition.

Declaration of competing interest

The authors declare that they have no known competing financial interests or personal relationships that could have appeared to influence the work reported in this paper.

Acknowledgements

OA acknowledge financial support from the Royal Society of Chemistry through E22-7965264821, The Royal Society through RG\R2\232243 and the Engineering and Physical Sciences Research Council (EPSRC) through EP /X029956/1. OJA acknowledges the financial support from the Royal Society of Chemistry through R23-6478073709 and the Royal Society through RG\R2\232090. NND and KO acknowledges financial support from the Leverhulme Trust through RC-2015-011. ZY thanks UKRI NERC Fellowship grant (NE/R013349/2) and Leverhulme Trust Research Leadership Awards (RL-2022-041). The authors thank the School of Science and Engineering, University of Dundee for electron microscopy and X-ray diffraction analysis.

Appendix B. Supplementary data

Supplementary data to this article can be found online at https://doi.org/10.1016/j.talanta.2024.127400.

Data availability

Data will be made available on request.

References

[1] J. Riss, J. Cloyd, J. Gates, S. Collins, Benzodiazepines in epilepsy: pharmacology and pharmacokinetics, Acta Neurol. Scand. 118 (2008) 69–86, https://doi.org/10.1111/j.1600-0404.2008.01004.x.
[2] D.A. Ciraulo, E.P. Nace, Benzodiazepine treatment of anxiety or insomnia in substance abuse patients, Am. J. Addict. 9 (2000) 276–284, https://doi.org/10.1080/105504900750047346.
[3] A. Maguire, I. Douglas, L. Smeeth, M. Thompson, Determinants of cholesterol and triglycerides recording in patients treated with lipid lowering therapy in UK primary care, Pharmacoepidemiol, Drug Saf. 16 (2007), https://doi.org/10.1002/pds, 228–228.
[4] M.K. Ticku, T.P. Burch, W.C. Davis, The interactions of ethanol with the benzodiazepine-GABA receptor-ionophore complex, Pharmacol. Biochem. Behav. 18 (1983) 15–18, https://doi.org/10.1016/0091-3057(83)90140-5.
[5] S.L. Dalterio, M.J. Wayner, I. Geller, R.J. Hartmann, Interactive effects of diazepam and ethanol on baboon match-to-sample performance, Alcohol 5 (1988) 477–480, https://doi.org/10.1016/0741-8329(88)90086-9.
[6] I.J. Bosman, M. Verschraagen, K.J. Lusthof, Toxicological findings in cases of sexual assault in The Netherlands, J. Forensic Sci. 56 (2011) 1562–1568, https://doi.org/10.1111/j.1556-4029.2011.01888.x.
[7] A.W. Jones, A. Holmgren, J. Ahlner, Toxicological analysis of blood and urine samples from female victims of alleged sexual assault, Clin. Toxicol. 50 (2012) 555–561, https://doi.org/10.3109/15563650.2012.702217.
[8] A.E. Almeida, M.L. Ribeiro, L. Polese, Determination of amfepramone hydrochloride, fenproporex, and diazepam in so-called "natural" capsules used in the treatment of obesity, J. Liq. Chromatogr. Relat. Technol. 23 (2000) 1109–1118, https://doi.org/10.1081/JLC-100101512.
[9] P. Ghosh, M.M.K. Reddy, V.B. Ramteke, B.S. Rao, Analysis and quantitation of diazepam in cream biscuits by high-performance thin-layer chromatography and its confirmation by mass spectrometry, Anal. Chim. Acta 508 (2004) 31–35, https://doi.org/10.1016/j.aca.2003.11.058.
[10] K.C. Honeychurch, A. Crew, H. Northall, S. Radbourne, O. Davies, S. Newman, J. P. Hart, The redox behaviour of diazepam (Valium®) using a disposable screen-printed sensor and its determination in drinks using a novel adsorptive stripping voltammetric assay, Talanta 116 (2013) 300–307, https://doi.org/10.1016/j.talanta.2013.05.017.
[11] E. Mikami, T. Goto, T. Ohno, H. Oka, H. Kanamori, Simultaneous analysis of seven benzodiazepines in dietary supplements as adulterants using high performance liquid chromatography and its application to an identification system for diazepam, J. Heal. Sci. 51 (2005) 278–283, https://doi.org/10.1248/jhs.51.278.
[12] M. Acikkol, S. Mercan, S. Karadayi, Simultaneous determination of benzodiazepines and ketamine from alcoholic and nonalcoholic beverages by GC-MS in drug facilitated crimes, Chromatographia 70 (2009) 1295–1298, https://doi.org/10.1365/s10337-009-1278-6.
[13] V. Prakash, S. Sharma, J. Kaur, S.K. Mehta, Graphene oxide/lysine composite-a potent electron mediator for detection of diazepam, Anal. Methods 10 (2018) 5038–5046, https://doi.org/10.1039/c8ay01429a.
[14] M.R. Milani Hosseini, A. Motaharian, Electroanalytical determination of diazepam in tablet and human serum samples using a multiwalled carbon nanotube embedded molecularly imprinted polymer-modified carbon paste electrode, RSC Adv. 5 (2015) 81650–81659, https://doi.org/10.1039/c5ra11598a.
[15] R. Webb, P. Doble, M. Dawson, A rapid CZE method for the analysis of benzodiazepines in spiked beverages, Electrophoresis 28 (2007) 3553–3565, https://doi.org/10.1002/elps.200700110.
[16] G. Magdy, N. Said, R.A. El-Domany, F. Belal, Nitrogen and sulfur-doped carbon quantum dots as fluorescent nanoprobes for spectrofluorimetric determination of olanzapine and diazepam in biological fluids and dosage forms: application to content uniformity testing, BMC Chem 16 (2022) 1–15, https://doi.org/10.1186/s13065-022-00894-y.
[17] D.S.M. Ribeiro, J.A.V. Prior, J.L.M. Santos, J.L.F.C. Lima, Diazepam fluorimetric monitoring upon photo-degradation in an automatic miniaturized flow system, J. Fluoresc. 20 (2010) 915–922, https://doi.org/10.1007/s10895-010-0637-x.
[18] C.M. Niemeyer, Biotechnology meets materials science, Mater. Sci. 40 (2001) 4128–4158. http://www3.interscience.wiley.com/journal/88012836/abstract.
[19] H. Huang, J.J. Zhu, The electrochemical applications of quantum dots, Analyst 138 (2013) 5855–5865, https://doi.org/10.1039/c3an01034a.
[20] M. Wan, A. Jimu, H. Yang, J. Zhou, X. Dai, Y. Zheng, J. Ou, Y. Yang, J. Liu, L. Wang, MXene quantum dots enhanced 3D-printed electrochemical sensor for the highly sensitive detection of dopamine, Microchem. J. 184 (2023) 108180, https://doi.org/10.1016/j.microc.2022.108180.
[21] A. Fakhri, M. Naji, S. Tahami, Ultraviolet/ultrasound-activated persulfate for degradation of drug by zinc selenide quantum dots: catalysis and microbiology study, J. Photochem. Photobiol. B Biol. 170 (2017) 304–308, https://doi.org/10.1016/j.jphotobiol.2017.04.024.

[22] Z. Ali, M. Hassan Sayyad, A. Ali, M. ur Rahman, N. Anwar, S. Khan, Study on the photovoltaic characteristics of solar cells based on PbS quantum dots and carbon counter electrode, Mater. Sci. Eng. B 301 (2024) 117144, https://doi.org/10.1016/j.mseb.2023.117144.
[23] M. Deo, R.K. Chauhan, M. Kumar, A synergistic approach in designing InP/ZnS quantum dot based CIGS solar cell, Micro and Nanostructures 185 (2024) 207710, https://doi.org/10.1016/j.micrna.2023.207710.
[24] B. Mohanty, L. Giri, B.K. Jena, MXene-Derived quantum dots for energy conversion and storage applications, Energy Fuel. 35 (2021) 14304–14324, https://doi.org/10.1021/acs.energyfuels.1c01923.
[25] Y. Sun, Q. Dong, H. Yang, W. Song, H. Zhou, CuS quantum dots activated DNAzyme for ratiometric electrochemical detection of telomerase activity, Anal. Chim. Acta 1248 (2023) 340884, https://doi.org/10.1016/j.aca.2023.340884.
[26] F. Shahdost-fard, M. Roushani, Cu-In-S/ZnS quantum dots/silver nanoparticles nanocomposites-modified electrode as an electrochemical label-free aptasensor for the detection of β-casomorphin 7 in early distinguish of autism, Microchem. J. 159 (2020) 105514, https://doi.org/10.1016/j.microc.2020.105514.
[27] Y. Liu, L. Wang, H. Li, L. Zhao, Y. Ma, Y. Zhang, J. Liu, Y. Wei, Rigorous recognition mode analysis of molecularly imprinted polymers—rational design, challenges, and opportunities, Prog. Polym. Sci. 150 (2024) 101790, https://doi.org/10.1016/j.progpolymsci.2024.101790.
[28] S. Ansari, S. Masoum, Recent advances and future trends on molecularly imprinted polymer-based fluorescence sensors with luminescent carbon dots, Talanta 223 (2021) 121411, https://doi.org/10.1016/j.talanta.2020.121411.
[29] K. Khadem-Abbassi, H. Rinnert, L. Balan, Z. Doumandji, O. Joubert, M. Masteri-Farahani, R. Schneider, CdTe0.5s0.5/zns quantum dots embedded in a molecularly imprinted polymer for the selective optosensing of dopamine, Nanomaterials 9 (2019), https://doi.org/10.3390/nano9050693.
[30] X. Hu, Y. Zhao, J. Dong, C. Liu, Y. Qi, G. Fang, S. Wang, A strong blue fluorescent nanoprobe based on Mg/N co-doped carbon dots coupled with molecularly imprinted polymer for ultrasensitive and highly selective detection of tetracycline in animal-derived foods, Sensors Actuators, B Chem. 338 (2021), https://doi.org/10.1016/j.snb.2021.129809.
[31] K. Oyinlola, K.O. Adeniyi, N. Nic Daeid, O. Adegoke, Heavy metal-free MnInPSeS alloyed quantum dots-molecularly imprinted polymer as an electrochemical nanosensor for the detection of the synthetic cathinone, 3,4-methylenedioxypyrovalerone, Mater. Sci. Semicond. Process. 183 (2024) 108750, https://doi.org/10.1016/j.mssp.2024.108750.
[32] X. Wang, G. Li, J. Peng, X. Lai, Q. Wu, Y. Cao, L. Ding, J. Tu, The Au/ZnSe/ZnO heterojunction improves the electron transfer behavior to enhance the detection performance of ascorbic acid, J. Alloys Compd. 873 (2021) 159721, https://doi.org/10.1016/j.jallcom.2021.159721.
[33] X.Z. Song, W.Y. Zhu, X.F. Wang, Z. Tan, Recent advances of CeO2-based electrocatalysts for oxygen and hydrogen evolution as well as nitrogen reduction, Chemelectrochem 8 (2021) 996–1020, https://doi.org/10.1002/celc.202001614.
[34] O. Adegoke, M.L. Nsuamani, N. Nic Daeid, Cadmium-free silica-encapsulated molecularly imprinted AuZnCeSeS quantum dots nanocomposite as an ultrasensitive fluorescence nanosensor for methamphetamine detection, Mater. Sci. Semicond. Process. 159 (2023) 107387, https://doi.org/10.1016/j.mssp.2023.107387.
[35] O. Adegoke, H. Montaseri, S.A. Nsibande, P.B.C. Forbes, Passivating effect of ternary alloyed AgZnSe shell layer on the structural and luminescent properties of CdS quantum dots, Mater. Sci. Semicond. Process. 90 (2019), https://doi.org/10.1016/j.mssp.2018.10.025.
[36] P. Yomthiangthae, T. Kondo, O. Chailapakul, W. Siangproh, The effects of the supporting electrolyte on the simultaneous determination of vitamin B2, vitamin B6, and vitamin C using a modification-free screen-printed carbon electrode, New J. Chem. 44 (2020) 12603–12612, https://doi.org/10.1039/d0nj02175j.
[37] O. Adegoke, S. Zolotovskaya, A. Abdolvand, N. Nic Daeid, Fabrication of a near-infrared fluorescence-emitting SiO2-AuZnFeSeS quantum dots-molecularly imprinted polymer nanocomposite for the ultrasensitive fluorescence detection of levamisole, Colloids Surf. A Physicochem. Eng. Asp. 646 (2022) 129013.
[38] N. Shams, H.N. Lim, R. Hajian, N.A. Yusof, J. Abdullah, Y. Sulaiman, I. Ibrahim, N. M. Huang, A. Pandikumar, A promising electrochemical sensor based on Au nanoparticles decorated reduced graphene oxide for selective detection of herbicide diuron in natural waters, J. Appl. Electrochem. 46 (2016) 655–666, https://doi.org/10.1007/s10800-016-0950-4.
[39] D.S.M. Ribeiro, J.A.V. Prior, J.L.M. Santos, J.L.F.C. Lima, Automated determination of diazepam in spiked alcoholic beverages associated with drug-facilitated crimes, Anal. Chim. Acta 668 (2010) 67–73, https://doi.org/10.1016/j.aca.2010.01.016.
[40] M.A. Zare, M.S. Tehrani, S.W. Husain, P.A. Azar, Multiwall carbon nanotube-ionic liquid modified paste electrode as an efficient sensor for the determination of diazepam and oxazepam in real samples, Electroanalysis 26 (2014) 2599–2606, https://doi.org/10.1002/elan.201400305.

DSPACE

https://dspace.org/

An organic-inorganic polyacrylamide-based surface imprinted quantum dots for the impedimetric and voltammetric detection of diazepam in saliva with smartphone readout

Adegoke, Oluwasesan; Oyinlola, Kayode; Adeniyi, Kayode Omotayo; Achadu, Ojodomo J; Yang, Zhugen ...

2025-04-01
Elsevier
https://doi.org/10.1016/j.talanta.2024.127400
Adegoke O, Oyinlola K, Adeniyi KO. (2025) An organic-inorganic polyacrylamide-based surface imprinted quantum dots for the impedimetric and voltammetric detection of diazepam in saliva with smartphone readout. Talanta, Volume 285, April 2025, Article number 127400

Downloaded from a DSpace repository. https://dspace.org/